# Large Eddy Simulation of an Initially-Confined Triangular Oscillating Jet

**Minyi Xu · Jianchun Mi · Pengfei Li**

**Abstract** This paper reports the first large eddy simulation (LES) of a self-excited oscillating triangular jet (OTJ) issuing from a fluidic nozzle that consists of a small triangular orifice inlet followed by a large circular chamber and an orifice outlet. The case simulated is identical to that measured experimentally by England et al. (Exp Fluids 48(1):69–80, 2010). The present prediction agrees well with the previous measurement. The simulation reveals that the central oscillating jet exhibits axis-switching in the cross-section and rotates by 60° approximately over a downstream distance of $x = 0.5D$ (chamber diameter). Three strong longitudinal vortices occur associated with the three vertices of the inlet triangle. These vortices strongly interact with the central jet and also the surroundings, in the region at $x/D \leq 1$, and appear to merge finally with the outer secondary swirling flow. These observations are consistent with the deduction from previous experiments.

**Keywords** Large eddy simulation · Self-excited oscillation · Turbulent jet · Coherent structure

## 1 Introduction

A small flow ejecting into a relatively large specific chamber can produce large-scale low-frequency oscillations—this flow is complex and termed as a self-excited oscillating jet. (The corresponding device is often named as *Fluidic Nozzle*). Compared with relatively simple, non-oscillating, free jets, e.g. round or triangular jets, the self-excited oscillating jet produces greater spreading rate, higher velocity decay rate and larger-scale velocity fluctuations which are all a source of large-scale turbulent mixing [1–6]. Such flows may be used to improve the performance of industrial burners, multi-media mixers and reactors in the processing industry. For example, a great number

M. Xu · J. Mi (✉) · P. Li
State Key Laboratory of Turbulence and Complex Systems, College of Engineering,
Peking University, Beijing 100871, China
e-mail: jcmi@coe.pku.edu.cn

of the self-excited precessing jet (PJ) devices [1] and, more generally, oscillating-jet devices [2] have been beneficially installed at cement, glass and lime kilns [3].

In early studies with a circular orifice, Nathan et al. [4] showed that, for the precessing jet to oscillate reliably, the chamber inlet-expansion ratio must be larger than about 5.0, i.e. $D/d_{e1} > 5$ (see Fig. 1 for notations), and the length-to-diameter ratio of the chamber must be in the range $2.6 \leq L/D \leq 2.8$. A small lip of height $h_2 = (D - d_2)/2 \leq 0.1D$ is usually attached to the chamber exit. Measurements and observations of the precessing jet [5, 6] show that the Strouhal number of the precession has a significant influence on the oscillating mixing field, while the Reynolds number does not, provided that it is sufficiently high.

Mi et al. [2] then found that the non-circular orifice can enhance the oscillation process, relative to the circular inlet case. In particular, the use of the triangular inlet is one of the best options for this enhancement. In a parametric study of the oscillating triangular jet (OTJ) nozzle, Lee [7, 8] and Lee et al. [7, 8] found that the spreading angle of the OTJ flow from the nozzle is significantly smaller than that of the PJ flow and it varies more gradually over broad ranges of the ratios $L/D$ and $D/d_{e1}$. A designer therefore has the flexibility not only to accommodate a much lower supply pressure but also to choose the jet spreading angle. England et al. [9] investigated the effect of the density ratio of the OTJ fluid to ambient fluid on the resulting OTJ flow downstream from the nozzle. The initial spread and decay of the emerging jet were found to depend upon the density ratio while the dominant oscillation frequency decreases with increasing the density ratio.

Lee [7] performed measurements of the surface flow pressure and of the vortex patterns in the plane transverse to the dominant direction of flow. He used this to propose a vortex skeleton and a mechanism for the oscillation. However, the OTJ flow is highly unsteady and complex, so that much detailed information on the instantaneous flow structure inside the chamber is still lacking. This makes it difficult to fully understand the formation mechanism of the oscillation. The present work is part of the study whose objective is to eventually address this deficit. We use Large Eddy Simulation (LES) to visualize the in-chamber OTJ flow structure. Note that the LES, once validated, can provide the quantitative and three-dimensional detail of the whole flow, which remains unrealistic to determine by experiments. To our best knowledge, this is the first study of the OTJ flow by LES.



**Fig. 1** A schematic diagram of the OTJ nozzle showing notation. Here $d_{e1} = D/3.5$ and $d_2 = 0.82D$
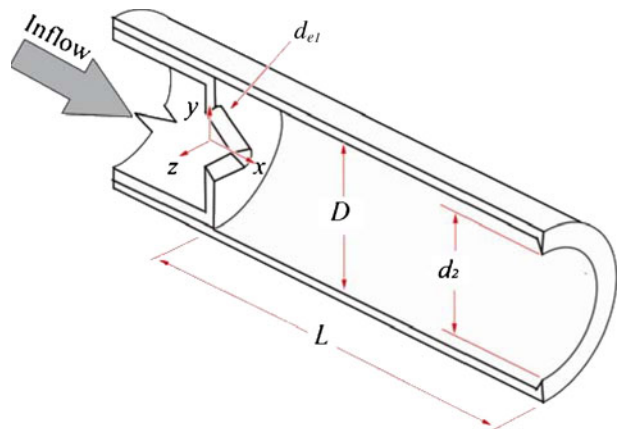
Following the experimental investigations by England et al. [9] on the OTJ flow, the present study is aimed at examining both the mean and instantaneous OTJ flow structures mainly inside the chamber under the same initial and boundary conditions. The simulation was performed for $Re_1 = 17,900$, the same Reynolds number as for the flow of England et al. [9], where $Re_1 \equiv U_1 d_{e1}/v$ with $U_1$ being the mass-averaged velocity at the orifice-inlet, $d_{e1}$ the orifice equivalent diameter and $v$ the kinematic viscosity of the fluid.

## 2 Computational Details

The spatially filtered governing equations of an unsteady incompressible viscous flow for LES are

$$\frac{\partial \bar{u}_i}{\partial t} + \frac{\partial \bar{u}_i \bar{u}_j}{\partial x_j} = -\frac{\partial \bar{p}}{\partial x_i} + \frac{1}{Re_1} \frac{\partial^2 \bar{u}_i}{\partial x_j \partial x_j} - \frac{\partial \tau_{ij}}{\partial x_j} \tag{1}$$

$$\frac{\partial \bar{u}_i}{\partial x_i} = 0 \tag{2}$$

where $x_i$ $(i = 1, 2, 3)$ are the coordinates, as replaced later by $(x, y, z)$, $\bar{u}_i$ are the corresponding spatially filtered velocity components and $\bar{p}$ is the spatially filtered pressure. The subgrid-scale stress (SGS) tensor $\tau_{ij}$, defined by

$$\tau_{ij} = \overline{u_i u_j} - \bar{u}_i \bar{u}_j \tag{3}$$

which was modeled by Smagorinsky as

$$\tau_{ij} - \frac{\delta_{ij}}{3} \tau_{kk} = -2 v_t \overline{S}_{ij}. \tag{4}$$

In Eq. 4, $\delta_{ij}$ is Kronecker's delta, and $v_t$ is the eddy viscosity, and $\overline{S}_{ij}$ is the resolved scale strain rate tensor, defined as

$$\overline{S}_{ij} = \frac{1}{2} \left( \frac{\partial \bar{u}_i}{\partial x_j} + \frac{\partial \bar{u}_j}{\partial x_i} \right) \tag{5}$$

whose magnitude can also be defined by

$$|\bar{S}| = \sqrt{2 \overline{S}_{ij} \overline{S}_{ij}}. \tag{6}$$

The dynamic sub-grid stress model for the eddy viscosity is

$$v_t = C \Delta^2 \left| \overline{S} \right| \tag{7}$$

where $\Delta$ is the grid filter width computed according to the volume of the computational cell using $\Delta = V^{1/3}$ and $C$ is a coefficient. The concept of the dynamic procedure is to apply a second filter (called the test filter) to the equations of motion. The new filter width $\hat{\Delta}$ is equal to twice the grid filter width $\Delta$. Both filters produce a resolved flow field. The difference between the two resolved fields is the contribution of the small scales whose size is in between the grid filter and the test filter.

At the test filtered field level, the sub-test scale stress tensor can be expressed as

$$T_{ij} = \widehat{\overline{u_i u_j}} - \widehat{\overline{u}}_i \, \widehat{\overline{u}}_j. \tag{8}$$

If the sub-test scale stresses are parameterized, in a manner analogy to the sub-grid ones, by

$$T_{ij} - \frac{\delta_{ij}}{3} T_{kk} = -2C\widehat{\Delta}^2 \left| \widehat{\overline{S}} \right| \widehat{\overline{S}}_{ij} \tag{9}$$

In Eqs. 7 and 9, the coefficient $C$ is assumed to be the same and independent of the filter process. The sub-grid stress and the sub-test scale stress are related by Germano et al. [10] as

$$L_{ij} = T_{ij} - \hat{\tau}_{ij} = \widehat{\overline{u}_i \overline{u}_j} - \widehat{\overline{u}}_i \, \widehat{\overline{u}}_j \tag{10}$$

where $L_{ij}$ is computable from the resolved large eddy filed. Substitution of Eqs. 4 and 9 into Eq. 10, requiring that the error be minimized in the least-squares sense [11], gives

$$C = \frac{\left( L_{ij} - L_{kk}\delta_{ij}/3 \right)}{M_{ij}M_{ij}} \tag{11}$$

with

$$M_{ij} = -2 \left( \widehat{\Delta}^2 \left| \widehat{\overline{S}} \right| \widehat{\overline{S}}_{ij} - \Delta^2 \widehat{\left| \overline{S} \right| \overline{S}_{ij}} \right) \tag{12}$$

The model constant $C$ in Eq. 11 is a local value, varying with time and space in a fairly wide range, and the negative $C$ together with the resultant negative eddy-viscosity is often interpreted as the 'back-scatter' transfer which describes the flow of energy from sub-grid scales to the resolved eddies. However, a too large negative eddy viscosity can cause numerical instability that can lead to the divergence. Therefore, $C$ is clipped at zero and 0.23 by default in FLUENT 6.3 [12]. Although this practice might be detrimental to the modeling accuracy, the dynamic SGS stress models can still properly predict the near-wall behavior of the SGS stress without any damping function or intermittency function. Because the SGS stress is proportional to the cube of the distance from the wall in the near-wall region, which is the correct asymptotic behavior for the SGS stress [10].

The incompressible LES Eqs. 1 and 2 were solved by a finite volume method based on the commercial computational software package Fluent 6.3 [12]. The central difference scheme was applied for spatial discretizations while the second-order three-level implicit scheme was used for time advancement. The SIMPLEC method was employed for the pressure-velocity coupling.

Figure 1 shows a schematic diagram of the OTJ nozzle used in present study and also by England et al. [9]. It comprises a circular chamber of diameter $D = 26.5$ mm and length $L = 2.5D$ with an equally triangular inlet of equivalent diameter $d_{e1} = D/3.5$ and chamber exit diameter $d_2 = 0.82D$. The OTJ nozzle is connected to a smooth straight pipe of internal diameter $D_o = 0.75D$, and length $L_o = 2D$. Here $x$, $y$ & $z$ denote the streamwise, spanwise and lateral directions, respectively. The origin of the coordinates is located at the centre of the triangular inlet.

To mimic the experimental case of England et al. [9], the velocity profile of a fully developed turbulent pipe flow was given upstream from the inlet at $x = -L_o$. That is, the velocity profile was determined by the empirical 1/7th power-law, i.e.,

$$U(r)/U_c = (1 - 2|r|/D_o)^{1/7} \tag{13}$$

where $U_c$ is the centerline velocity and $U(r)$ is the streamwise component of time-averaged velocity at radial distance, $r \equiv (y^2 + z^2)^{1/2}$, from the centerline of the pipe. At the pipe-inlet and the triangular orifice outlet, the bulk mean velocities are $U_j = 4.8$ m/s and $U_1 = 33.3$ m/s, respectively. In most experimental set-ups, background disturbances are usually present in flows of investigation. In the present study, we constructed the background disturbance such that its frequency spectrum consists of the Kolmogorov spectrum in the inertial region and the Pao spectrum in the dissipation region, respectively [13]. The background disturbance was randomly distributed in space at the jet inlet, and the amplitude (r.m.s. value) of the background disturbance was set to be $u_j = 0.01U_j$. Changes in the amplitude did not cause a significant change in the oscillation period. The no-slip boundary condition was applied at the nozzle surface. At the radial far-field boundary, a free-slip boundary condition was applied and a zero-gradient (Neumann) condition imposed on both of the inlet ($x = 0$) and outlet ($x = L$) sides.

The computational domain included the complete internal chamber and some external space of the nozzle, see Fig. 2a. The external region downstream from the chamber exit provided the needed 'buffer' region that was found important for the external near-field behavior of jet flows by Babu and Mahesh [14]. The downstream and side far-field boundaries of the computational domain were located at $30D$ downstream of triangular-inlet plane and $10D$ from the nozzle axis, respectively. A structured non-uniform grid arrangement was employed, see Fig. 2. The computational grid consisted of about 2 million cells with $160 (x) \times 112(y) \times 112(z)$ grid points. As shown in Fig. 2, the grid was clustered near the inner boundaries of the chamber to capture the high shear in that region. The grid resolution ($\Delta$) of the simulation is uniform, with $\Delta/D \approx 1/55.5$, along the chamber while it is varying, and $\Delta/D \approx 1/80$ on average, across the chamber. The resolution effect was checked by performing a new simulation at a higher resolution of $256 (x) \times 128(y) \times 128(z)$ grid points. The mean velocity data obtained by this simulation showed little difference due to the better resolution, e.g., see Fig. 4 for the centerline mean velocity; also, the difference in the oscillation frequency was less than 2%. This confirmed the grid independence of the solution.

The time step independence of solutions was tested, and the final time step selected was $5 \times 10^{-5}$ s, with which the oscillation frequency obtained became invariable. In each time-step a convergence criterion of $10^{-5}$ was used for the scaled residuals of the continuity equation. It is worth noting that the results of simulation became statically stationary when 20 global oscillations had occurred. The turbulent statistics were then made from the instantaneous data taken over next 60 global oscillation periods. Note as well that the collection time corresponds to approximately $22,700T_u$, where the time scale $T_u \equiv d_{e1}/U_1$. Computations in this paper were carried out on a HP Z800 workstation with 16 CPUs.
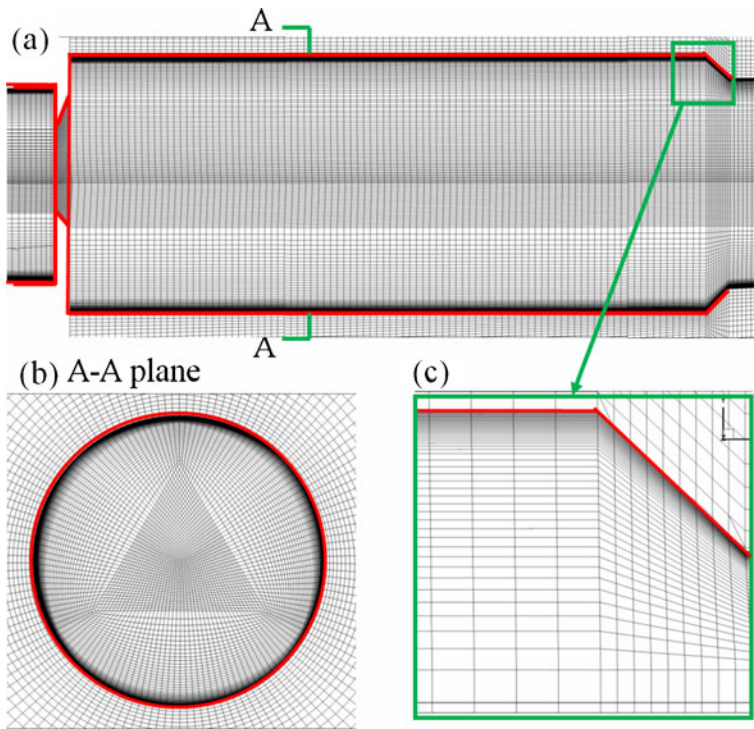
**Fig. 2** Grid distribution of calculation for the OTJ flow. **a** in the central *xy* plane ($z/D = 0$) of the chamber; **b** in the *yz* plane ($x/D = 1$) of the chamber; **c** zoom of grid distribution near the exit lip and chamber wall

## 3 Results and Discussion

The naturally oscillating triangular jet (OTJ) is highly unsteady and so its mean and instantaneous flow characteristics must be very different. In this section, we first verify the LES predictions using limited experimental data from England et al. [9] and then characterize respectively the mean and instantaneous OTJ flow fields produced by the LES modeling.

3.1 Experimental verification of the LES prediction

Based on the work of England et al. [9], a quantitative verification can be performed only through comparisons of the oscillation frequencies, centerline mean velocities and half-velocity widths obtained from the present simulation and the previous experiment [9].

The first check is provided to the oscillation frequency. Figure 3a shows the fluctuating velocity signals obtained at two locations near the chamber-exit lip, i.e., $x/D = 2.49$, $y/D = \pm 0.42$ and $z/D = 0$ while Fig. 3b compares the one-dimensional energy spectrum of the velocity signal, $u(t)$, from the upper location with that of the fluctuating pressure measured by England et al. [9] at the similar location. The energy spectrum is defined for the fluctuating velocity $u(t)$ measured at a
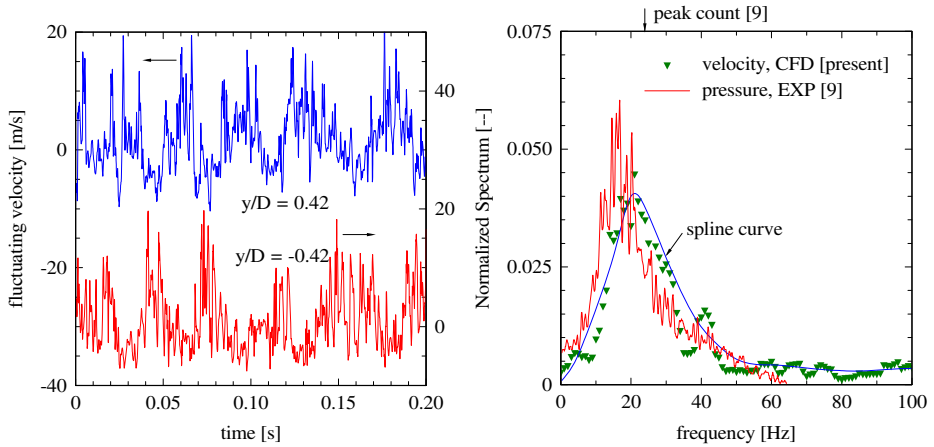
**Fig. 3** **a** Fluctuating velocity signals obtained at $x/D = 2.49$, $y/D = \pm 0.42$ and $z/D = 0$ and **b** the corresponding power spectrum for $y/D = 0.42$

single point as the Fourier transform of the autocorrelation given by $\Phi_u(f) = \int_{-\infty}^{\infty} e^{-j2\pi f\tau} R_{uu}(\tau)d\tau$, where $R_{uu}(\tau)$ is the autocorrelation function of $u(t)$, defined as $R_{uu}(\tau) = \int_{-\infty}^{\infty} u(t+\tau)u(t)dt$. Note that the present spectrum plotted is normalized by $<u^2>$. Obviously, both the present and previous spectra exhibit a broad peak, due to the jet oscillation, around which the average oscillation frequency ($f_p$) is expected to occur. (Note: the present data length of 52,000 samples for the fluctuating velocity was limited for the FFT calculation so that the corresponding spectrum (solid symbol) is somewhat scattering.) If we choose the frequency at which the spectrum is the highest as the true value of $f_p$, it is $f_p \approx 21$ Hz for the LES case and $f_p \approx 18$ Hz for the experiment [9]. (The frequency resolution for the simulation result is 1.0 Hz while the frequency resolution for experimental result is 0.2 Hz.) On the other hand, when applying a peak count method to signals (see Fig. 3a), the resulting frequency is $f_p \approx 25$ Hz for the present and $f_p \approx 24$ Hz for England et al. [9]; here the "peak count method" first counted the number ($N$) of broad peaks occurring in $u(t)$, due to the oscillation, over a duration $T$ and then obtained the oscillating frequency by $f_p = N/T$. Obviously, the use of the latter method results in a better agreement. This is expected since the latter method should be more accurate for the OTJ case. Relatively long time signals from a single location, from which the power spectrum is calculated through FFT, cannot capture all the jet oscillations occurring during the same time period, because the oscillating jet sometime takes the flip-flop (not rotational) mode and thus miss some locations near the chamber exit lip. Consequently, the broad peak in the spectrum occurs at a lower frequency than the true oscillation frequency. In conclusion, overall, the LES prediction of the oscillation frequency agree well with the measurement [9].

Next, a validation of the LES prediction is made here using both the centerline mean velocity ($U_c$) and half-velocity widths of the mean field ($y_{1/2}$, $z_{1/2}$), where $y_{1/2}$ and $z_{1/2}$ represent the lateral distances from the axis at which the local mean velocity is $U = 0.5U_c$. Figures 4 and 5 show respectively the centerline distribution of $U_1/U_c$ and the streamwise variations of $y_{1/2}/d_{eq}$ and $z_{1/2}/d_{eq}$ obtained from the present LES and from the previous PIV measurement downstream from the chamber outlet [9].

**Fig. 4** Centerline variation of the inverse mean velocity $U_1/U_c$
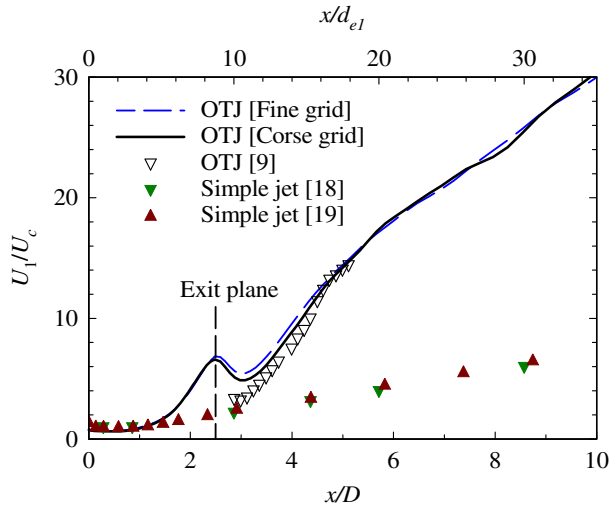


Note that these widths were calculated across the entire jet at several $x/D$ values and thus the average values of $y_{1/2}$ and $z_{1/2}$ on either side of the jet centerline are accounted. As seen in Figs. 4 and 5, in general, the LES predictions agree quite well with England et al.'s measurements of $U_1/U_c$ and $y_{1/2}/d$, at least, over the measured range $2.9 \leq x/D \leq 5.1$.

## 3.2 Characteristics of the mean OTJ flow field

### 3.2.1 Streamlines and contours of the mean velocity and pressure

To characterise the mean OTJ flow field, contours of the streamwise mean velocity calculated from the central $xy$-plane are shown in Fig. 6 whereas those from ten

**Fig. 5** Streamwise variations of half-velocity widths $y_{1/2}$ and $z_{1/2}$
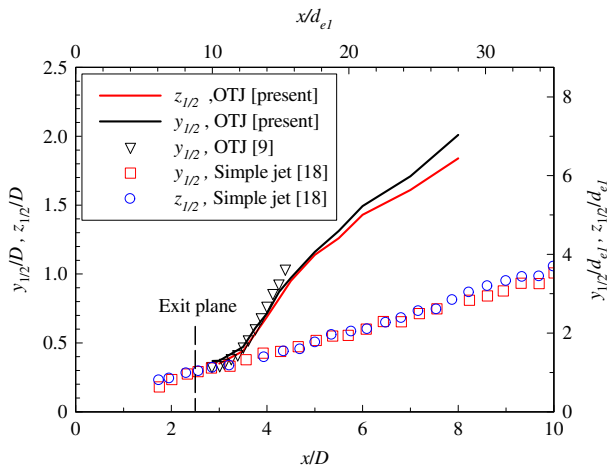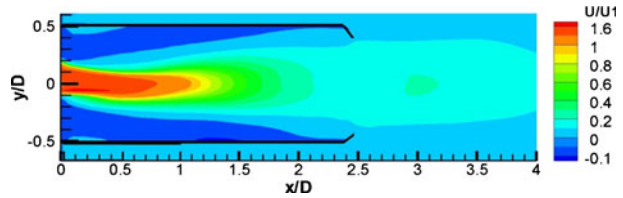
**Fig. 6** Contours of the
streamwise mean velocity in
the central $xy$-plane



different cross-sections of $x/D = 0.1 \sim 2.5$ inside and just outside the chamber are
displayed in Fig. 7a–j, together with cross-sectional views of the mean streamlines.
Note that the contours and streamlines were obtained by averaging the instantaneous
data over a time period of 60 cycles of the oscillation. Quite obviously from Fig. 6,
for $x/D \leq 1$ or $x/d_{e1} \leq 3.5$, the mean velocity ($U$) of the central jet is significantly
higher than the bulk-average velocity $U_1$ at the inlet; also, the inlet velocity takes the
maximum at the mid-way between the nozzle edge and the jet center (see Fig. 7a
and b). These observations are not unexpected because an orifice-type nozzle is
known to produce a three-dimensional "vena contracta" with such a distribution that
is relatively high in the central region and reaches the maximum somewhere between
the exit center and edge [15]. Besides, consistent with Lee [6], too, the mean OTJ flow
field in the $xy$ plane is asymmetric, see Fig. 6, due to the orientation of the triangular
exit (note: one apex and the mid-point of the base side are in the $xy$ plane).

Based on the mean velocity contours of Fig. 7, immediately downstream from the
inlet, at $x/D = 0.1$, the intensely spaced contours of the mean velocity $\geq 0.4U_1$ well
follow the exit triangular shape. As $x$ increases, the OTJ flow evolves significantly:
the jet cross-section appears to 'rotate' anti-clockwise approximately by 60° over a
distance of $x/D = 0.8$, exhibiting the 'axis-switching' phenomenon, which is often
referred to by investigators of noncircular free jets, see, e.g., Gutmark and Grinstein
[16]; Mi et al. [17]. Farther downstream ($x/D \geq 1.3$), the OTJ cross-section changes
little in shape. For $x/D \geq 2$, see Fig. 7g–h, the 'memory' of the initial triangular shape
of the OTJ is almost lost on average.

Based on the cross-sectional mean streamlines of Fig. 7, there exist three stream-
wise vortices, all rotating anti-clockwise, at each side of the exit 'triangle', in the
downstream region near the inlet. These vortical structures exist at least between
$x/D = 0.1$ and $x/D = 1.0$. As the flow proceeds downstream, they entrain and mix
with the surrounding fluid, thus becoming larger in size; concurrently, their strength
of rotation weakens. Evidently as well, these longitudinal structures move along with
the cross-sectional 'rotating triangle' sides. It is also revealed by the streamlines
that there is a secondary flow swirling anti-clockwise around the central jet inside
the chamber at $x/D \leq 1$. This swirl is quite strong at $x/D \leq 0.5$, with the mean
tangential velocity of up to $0.16U_1$ (see Fig. 8). It appears that the three vortices
spread out and merge with the outer swirl at $x/D \approx 1.3$ or $x/d_{e1} \approx 4.5$, around which
the unmixed core region is ended. Interestingly, the mean jet appears to spread out
radially from $x/D \geq 0.8$, reflecting the instantaneous jet deflection to the wall. This
deflection appears to make the OTJ to re-attach the wall at $x/D \approx 2.0$ followed by
its detaching, due to the presence of the outlet lip (diameter $d_2 = 0.82D$), toward the
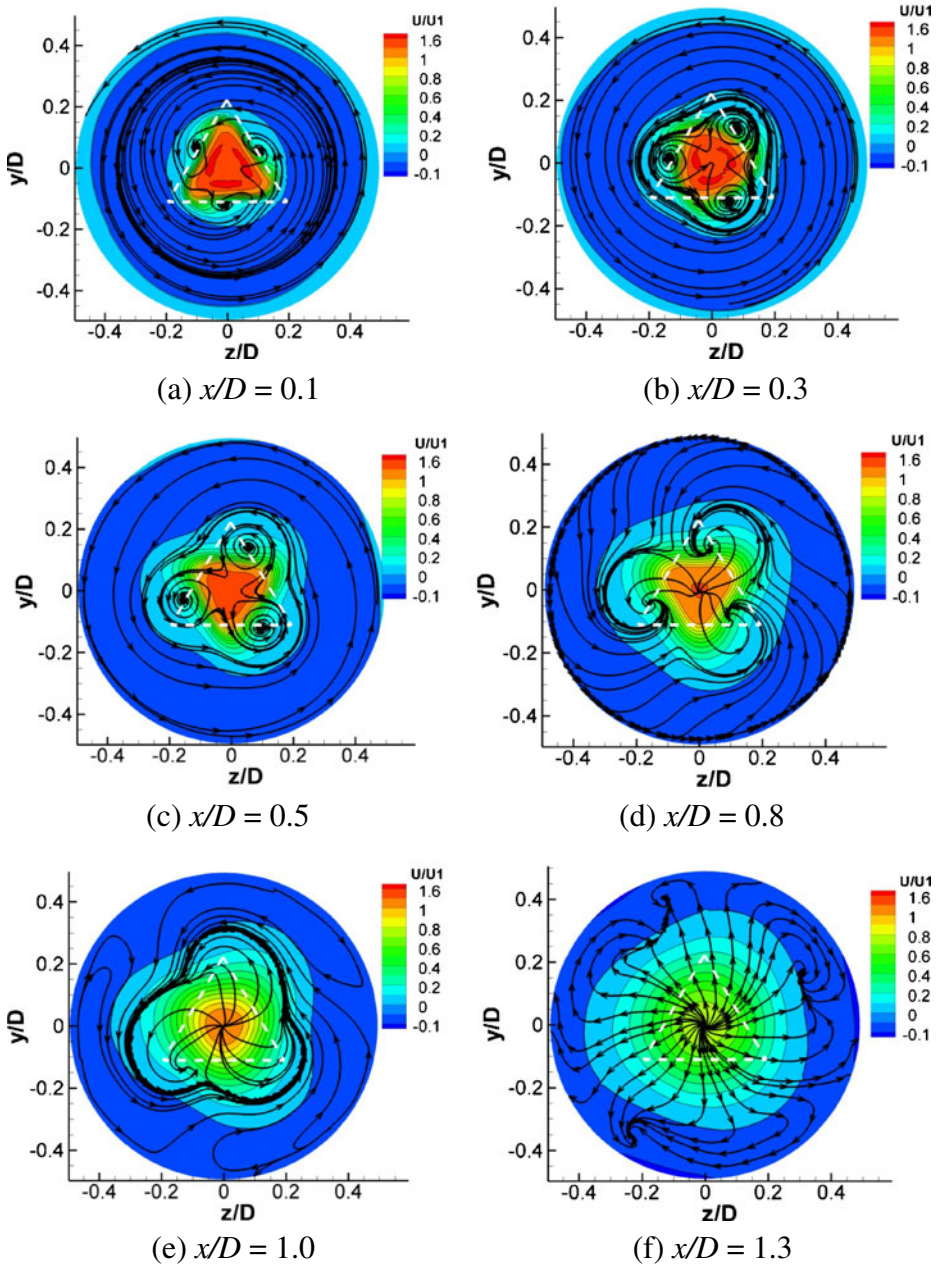other side and then discharging out of the chamber at $x/D = 2.5$. The interesting

**Fig. 7** Cross-sectional views of longitudinal mean velocity contours and mean streamlines at different $x/D$

pattern of the cross-sectional mean streamlines from $x/D = 2.2$ results from the dynamic interaction between the oscillating jet and inflowing fluid induced from the outside, with the presence of the outlet lip.
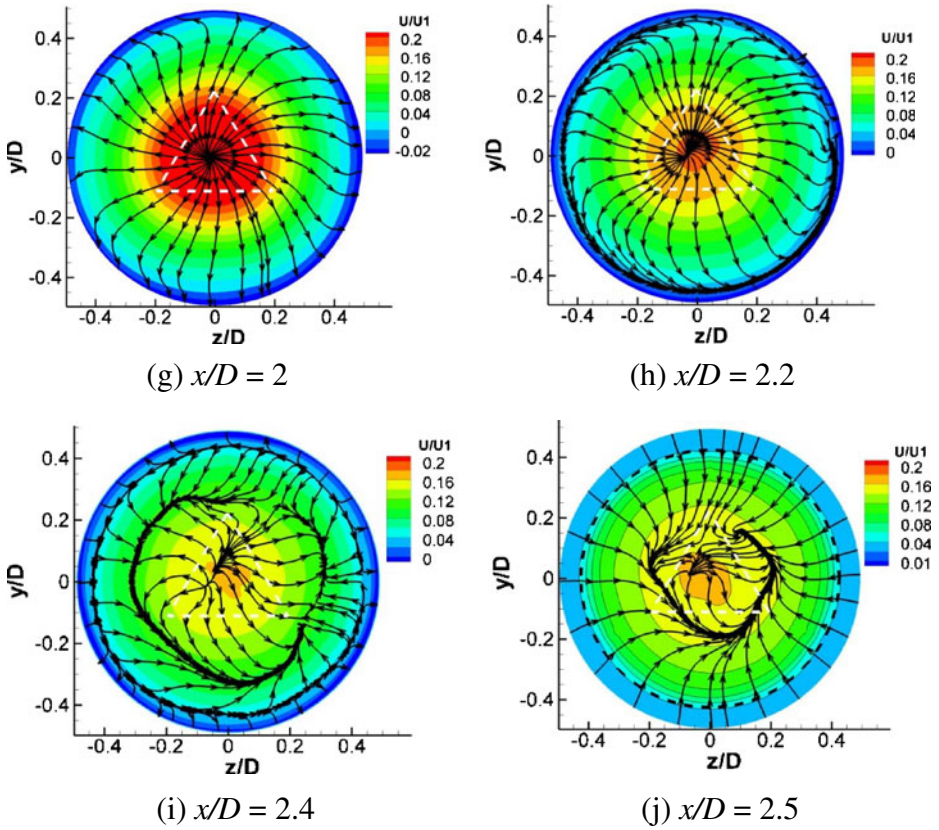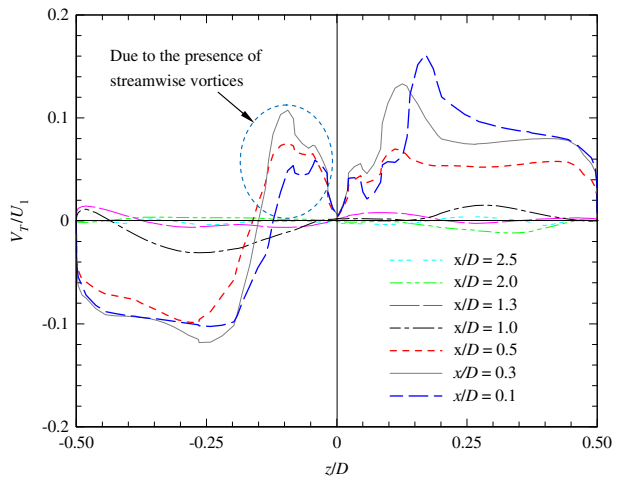
(g) x/D = 2

(h) x/D = 2.2

(i) x/D = 2.4

(j) x/D = 2.5

**Fig. 7** (continued)



**Fig. 8** Tangential velocity ($V_T$) distributions along the $z$ axis at $y = 0$ and different $x/D$

Through the outlet-lip plane, some ambient fluid is induced from the outside and interacts with the OTJ flow, forming a thin swirling interface (anti-clockwise for the present case). Near the outlet there is a backward flow just above the wall. Overall, Figs. 6 and 7 indicate that the in-chamber mean flow may be characterized by the central forward flow and outer low-speed backward flow (blue color contours) which occupies most of the inner space at $x/D \leq 1.0$. Perhaps noteworthy, some low-speed forward flow exists in a small space near the inner wall at $x/D \leq 0.5$ (see Fig. 6).

Figure 8 shows radial distributions of the tangential mean velocity ($V_T$) at $y = 0$ and $x/D = 0.1 \sim 2.5$. This velocity component is seen to be significant ($> 1$ m/s) at $r/D \geq 0.2$ and $x/D \leq 1.0$, indicating a strong anti-clockwise swirl in that region. It is also suggested that, for $x/D \leq 0.5$, the three streamwise vortices are very strong with $[V_T]_{max} \approx 0.1 U_1$ or beyond, which could correspond to an angular velocity of up to $2.4 \times 10^6$ rpm (2,000 times the oscillating frequency). For $x/D > 1.0$, the overall swirl becomes quite weak.

Figure 9 shows contours of the mean pressure coefficient $C_p \equiv 2(P_s - P_{atm})/(\rho U_1^2)$ at different $x/D$ inside the chamber, where $P_s$ and $P_{atm}$ are local static and ambient pressures, respectively. Consistent with earlier measurements by Lee [7] on the walls of the chamber, the overall static pressure inside the chamber is below ambient pressure. As a result, a certain amount of external fluid from outside is sucked into the chamber. Figure 9a–c demonstrate very clearly that the lowest static pressures are located at the centers of the streamwise vortices. This is expected because any vortex has lower pressure in the core region than outside; the higher the strength of rotation, the lower the core pressure. The highest static pressure zone is near to the inner wall along the entire chamber, where the absolute velocity is low. It is interesting to note as well that, in the chamber exit plane, the highest pressure (in red color) is aligned with the triangle apexes of the chamber inlet.

### 3.2.2 Centerline parameters and half-velocity widths

As indicated early in Fig. 4, the centerline mean velocity $U_c$ decreases monotonically inside the chamber ($x/D < 2.5$), then increases at $x/D < 3$ immediately downstream from the chamber exit, and decreases again farther downstream at $x/D > 3$. The increase over the region $2.5 < x/D < 3$ can be explained. At the exit plane of the chamber, a circular outlet lip of diameter $d_2 = 0.82D$ is placed with a backward-facing 45° ramp. The asymmetric jet emerging from the chamber therefore is deflected by the lip so that it passes across the nozzle axis in the near-field (centred at $0.5D$ downstream of the exit or $x/D = 3$), resulting in the centerline mean velocity being locally higher at $x/D < 3$.

Figure 5 shows the half-velocity widths ($y_{1/2}, z_{1/2}$) of the OTJ in the central $xy$ and $xz$ planes. It is demonstrated that both $y_{1/2}$ and $z_{1/2}$ increase monotonically with downstream distance. However, the growth of $y_{1/2}$ is faster than that of $z_{1/2}$ for $x/D > 5$. This is consistent with the oscillating triangular jet having preferred azimuthal zones of attachment aligned with the three sides, e.g., one in the $xy$ plane, as observed by Lee et al. [8]. Note that the jet flow precesses (i.e. rotates azimuthally) about the chamber axis in a continuously unstable manner.

Traditionally, the centerline variation of the mean velocity is used to measure the jet decay rate whereas the half-velocity width or radius reflects the jet spreading rate. For a general comparison between the oscillating and non-oscillating jets, previous hot-wire measurements of these properties in a free triangular jet by Quinn [18]
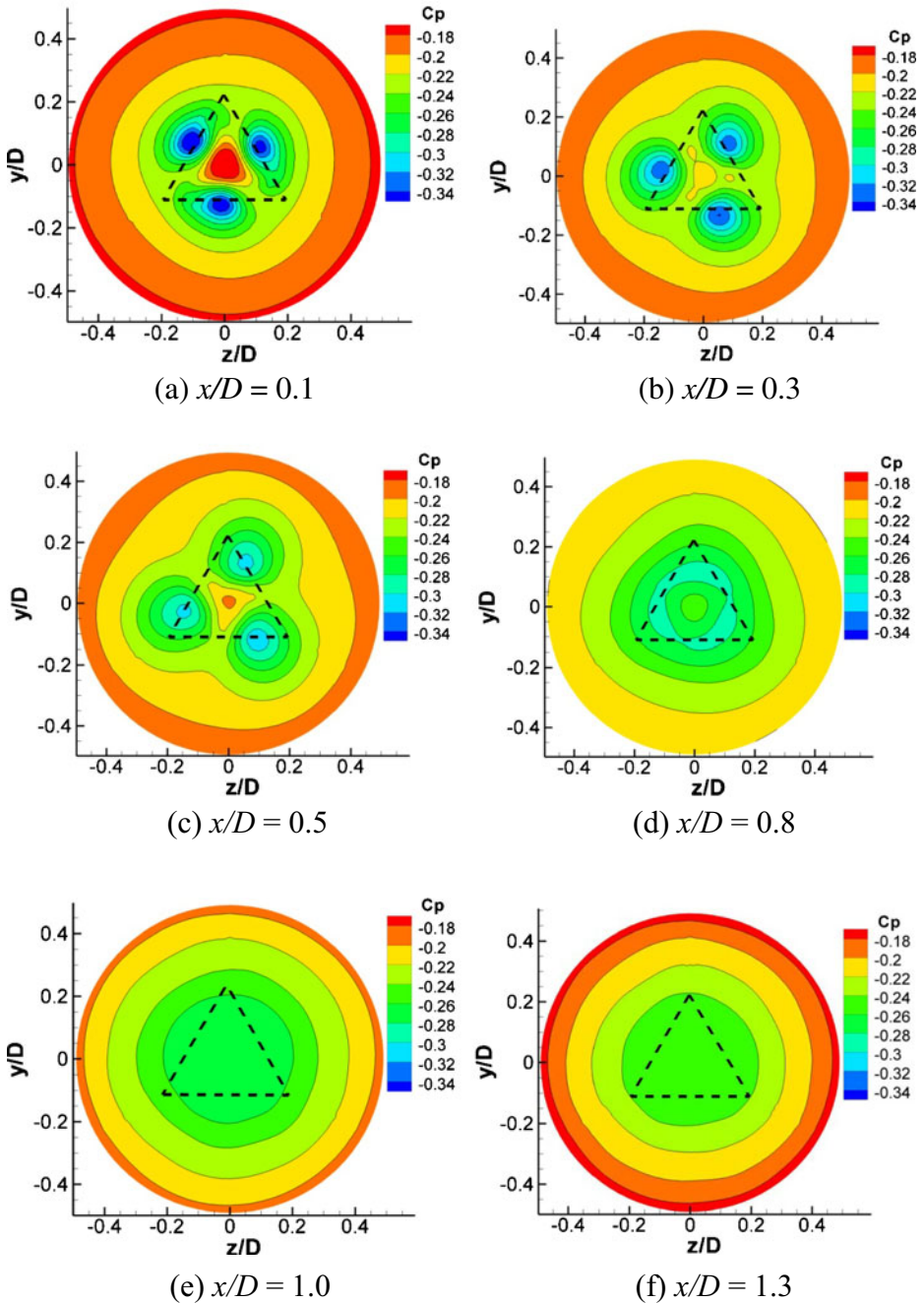
**Fig. 9** Cross-sectional contours of mean static pressure at different $x/D$

(g) $x/D = 2$

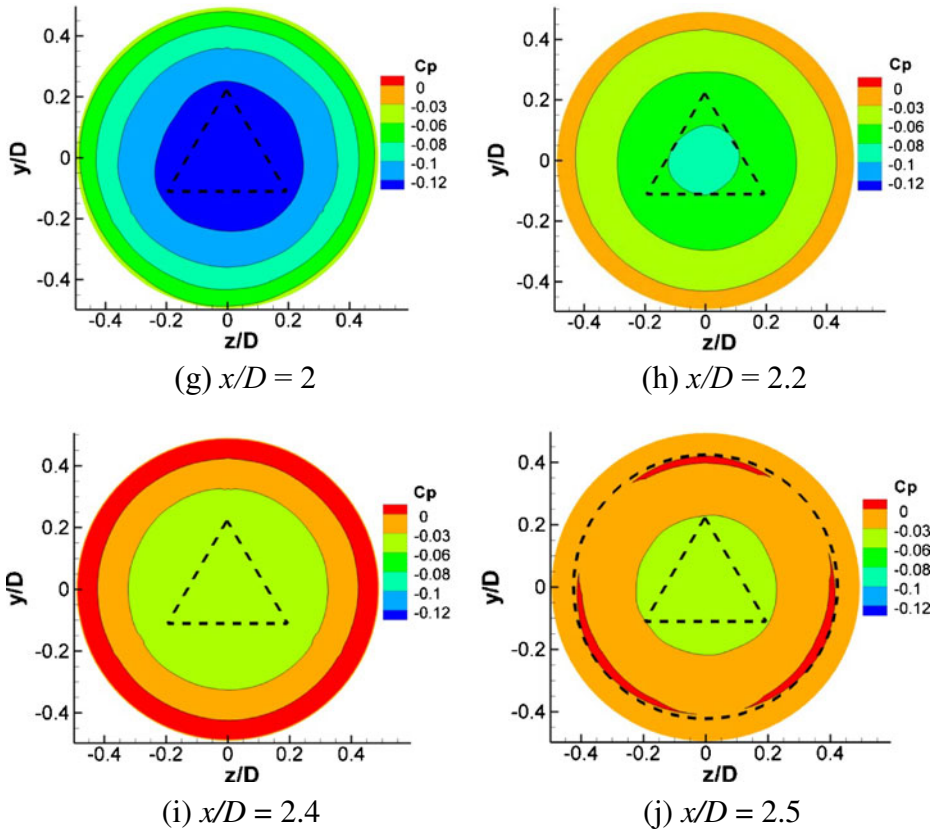(h) $x/D = 2.2$

(i) $x/D = 2.4$

(j) $x/D = 2.5$

**Fig. 9** (continued)

($Re_1 = 1.84 \times 10^5$) and Mi et al. [19] ($Re_1 = 1.5 \times 10^4$) are also presented in Figs. 4 and 5. Approximately, the overall decay and spread rates of the oscillating jet issuing from the fluidic nozzle of investigation are three to four times of those of the non-oscillating free jet. In other words, the presence of the low-frequency oscillation results in these rates being much higher for the partially confined oscillating jet. This, however, does not imply that the former jet has higher rates of mixing and entrainment. In fact, the investigation of Mi and Nathan [20] revealed the opposite case.

The low-frequency oscillation also causes the OTJ flow to exhibit a much higher 'turbulence intensity', compared with the case for the steady non-oscillating jet. (Note that the 'turbulence intensity' is traditionally defined as $\beta' \equiv < \beta^2 >^{1/2}$ where $\beta = u, v$ or $w$.) Figure 10 displays the centerline evolutions of the streamwise, lateral and spanwise turbulent intensities ($u', v', w'$). The result of $u'$ measured by Mi et al. [19] for the equilateral triangle jet is provided as the reference data. It is evident that, as $x$ increases, all the centerline turbulence intensities of the OTJ increase very rapidly and reach their maxima near to the chamber exit. More specifically, $[u'/U_c]_{max} \approx 1.24$ at $x/D = 2.27$ and $[v'/U_c]_{max} \approx [w'/U_c]_{max} \approx 0.95$ at $x/D = 2.5$, which are three to five times higher than that ($\approx 0.26$) obtained from the steady jet.

**Fig. 10** Centerline evolutions
of the turbulence intensities
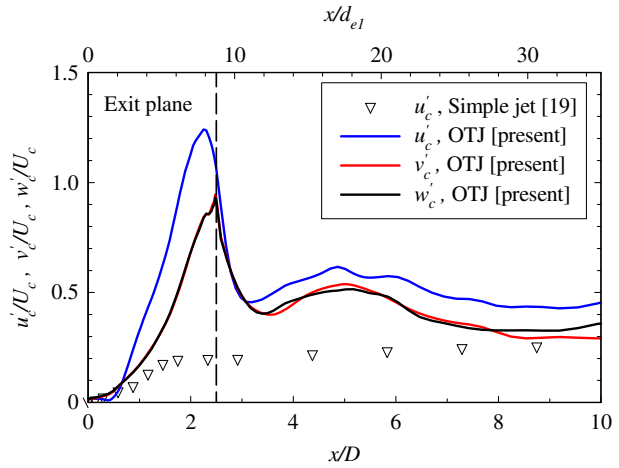


The relative intensities of the OTJ remain significantly higher even far downstream from the chamber; e.g., $u'/U_c \approx 0.4$, $v'/U_c \approx 0.3$ and $w'/U_c \approx 0.3$ at $x/D = 30$ or $x/d_{e1} = 105$. This implies that the impact of the initial oscillation is effective in the whole flow field. It is also observed that the streamwise turbulence intensity is always considerably higher than the lateral values. The latter observation coincides with previous PIV measurements of the non-oscillating jets [17].

Figure 11 shows the mean static pressure coefficient $C_p \equiv 2(P_s - P_{atm})/(\rho U_e^2)$ along the nozzle axis for the OTJ against the data of Quinn [18] obtained in a free triangular jet issuing from an orifice nozzle. It is evident that the variation trend of $P_s$ is similar for the two jets. For the free jet, the mean static pressure drops from a positive value (i.e., above atmospheric pressure) at the orifice exit to zero

**Fig. 11** Mean static pressure
variation on the centerline
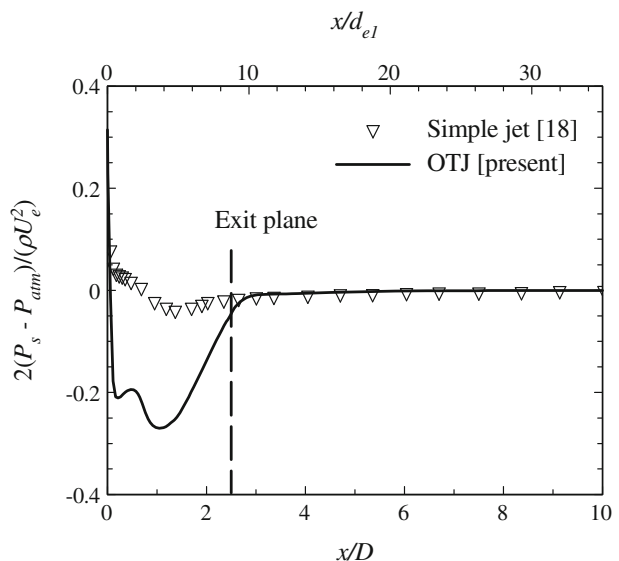
(i.e., at atmospheric pressure) as a result of the acceleration of the jet fluid brought about by the vena-contracta effect. The further decrease in $P_s$ to negative values (the minimum of $C_p \approx -0.05$) is triggered by the rapid production of turbulence from the mean flow shear and its redistribution, via the pressure fluctuations, in the near flow field. By comparison, for the OTJ flow, the confinement of the chamber makes the static pressure decrease greatly with the minimum of $C_p \approx -0.28$. Incidentally, the minimum pressure occurs near the end of the unmixed core for both jets.

3.3 Characteristics of the instantaneous OTJ flow

The typical instantaneous OTJ flow structure inside the chamber at a time instant is illustrated in Fig. 12a–c for the streamline projections in the central $xy$ and $xz$ planes and in different $yz$ planes. Figure 13 shows the evolution of cross-sectional views of streamlines and longitudinal velocity contours at $x/D = 2$ approximately within one oscillation period. Overall, it is demonstrated that the jet issuing from the triangular exit suddenly expands downstream into the chamber, re-attaches to the inner wall and oscillates continuously about the chamber axis due to natural instabilities (see, also, the fluctuating velocity signals of Fig. 3a). The oscillation appears to roughly take the mode of clockwise rotation (Fig. 13), accompanied by a swirling flow mainly anti-clockwise at $x/D \leq 1$ (Fig. 12c). The oscillating jet discharges out of the chamber into downstream 'unlimited' space. Simultaneously external ambient fluid is induced into the chamber and drawn upstream with some reverse fluid from the oscillating jet itself, forming the secondary flow swirling in the opposite sense to the oscillation. These flow characteristics are qualitatively consistent with experimental deductions [7]. However, the latter cannot display any similar instantaneous pictures inside a chamber due to the complexity of the OTJ flow and also the constraint of those optical measurement techniques.
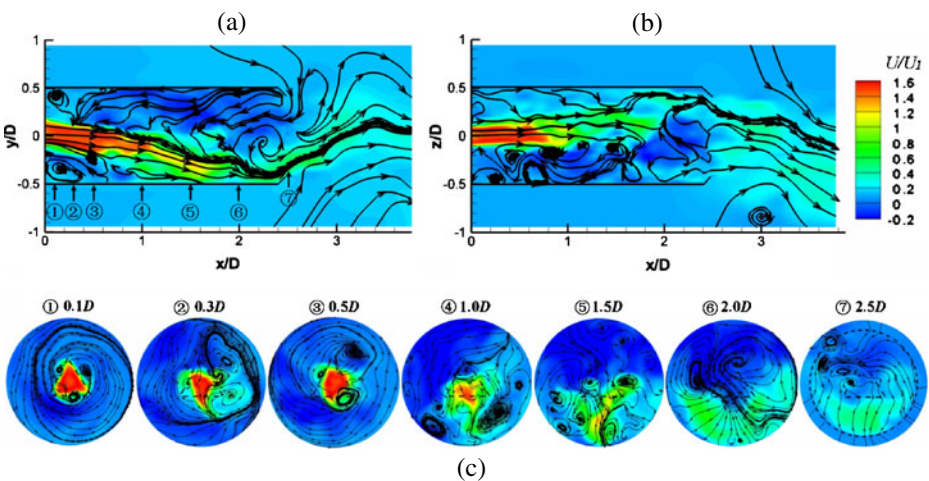


**Fig. 12** Projections of streamlines and streamwise velocity contours in **a** the central $xy$ plane, **b** the central $xz$ plane and **c** different $yz$ planes

(a) $t_0$ s      (b) $t_0$ +0.01s      (c) $t_0$ +0.02s      (d) $t_0$ +0.03s

(e) $t_0$ +0.04s      (f) $t_0$ +0.05s      (g) $t_0$ +0.06s
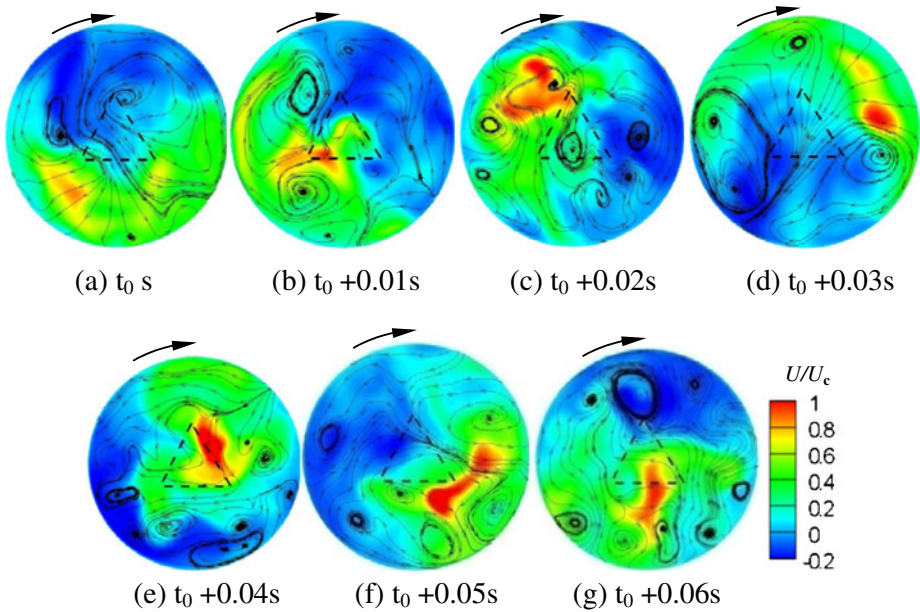
**Fig. 13** Evolution of cross-sectional views of streamlines and longitudinal velocity contours at $x/D = 2$ approximately within one oscillation period

Moreover, Fig. 12c reveals that three streamwise vortices are initially formed in conjunction with the exit triangle sides, interacting with each other and also with the central main jet. These are confirmed experimentally by Lee [7] through some conditional schemes. It appears that the three vortices spread out and merge with the outer swirl at $x/D \geq 1.0$. Interestingly, as well, several streamwise vortices occur at $x/D = 1.0 - 2.5$. In addition, a spanwise vortex is present around $x/D \approx 0.2$ in the upstream corner (see Fig. 12a and c).

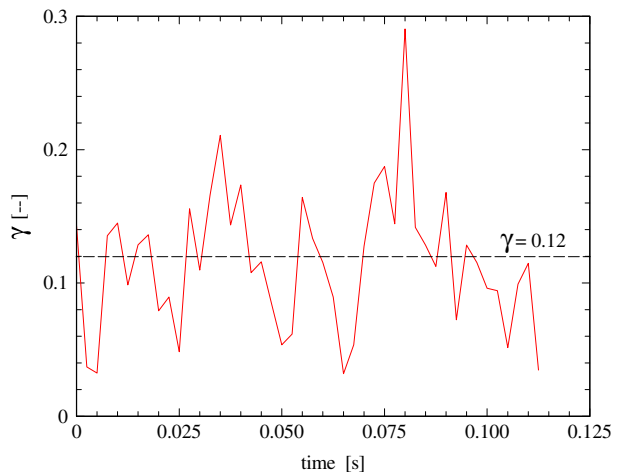**Fig. 14** Variation of forward-to-reverse flow rate with time at the chamber exit

Figure 13 displays that the main jet oscillates around the chamber axis in a clockwise rotation manner. However, the 'rotating' is poorly defined, occasionally with flip-flop motion, and thus not as regular as the precession of a jet issuing from a round inlet [3]. This difference has been observed in previous experimental investigations such as Lee [7]. This nature of the oscillation makes it difficult to determine precisely the oscillating frequency ($f_p$) by the frequency spectrum or other methods, as indicated early in Fig. 3. Nevertheless, based on short-interval consecutive images of the OTJ flow, we obtain that $f_p \approx 20$ Hz, slightly smaller than that estimated by the velocity spectrum. The corresponding Strouhal number defined by $St \equiv f_p d_{e1}/U_1$ is approximately 0.005 for the present LES. This $St$ is about two orders of magnitude lower than that of acoustically forced flow from a circular duct ($0.15 \leq St \leq 0.6$) [21] and a triangular duct ($St \approx 0.3$ and 0.51) [22].

For the instantaneous flow through the outlet plane, most of it exits out of the chamber while some is induced into the chamber from the outside, as clearly seen in Figs. 11, 12, and 13. The ratio of the instantaneous in-flowing to out-flowing flow rates at the exit plane is defined as

$$\gamma = \frac{Q_{in}}{Q_{out}} = \frac{\int_{A^-} u^- dA}{\int_{A^+} u^+ dA} \tag{14}$$

where $u^-$ and $A^-$ denote the inward-flow velocity and its corresponding area, and $u^+$ and $A^+$ stand for the outward-flow velocity and its corresponding area. Figure 14 shows the time variation of $\gamma$. Averaging $\gamma$ over the total time, we can obtain the mean ratio $\overline{\gamma} \approx 0.12$; that is, the inflow rate is 12% of the out-flow rate.

## 4 Concluding Remarks

The present study has used LES for the first time to simulate the oscillating triangular jet (OTJ) flow from a specific chamber described in Fig. 1 and Section 2. Predictions of the mean OTJ flow are quantitatively verified by recent measurements downstream of a similar chamber by England et al. [9], and the in-chamber flow structure is similar to Lee's measurements [7], even though both the Reynolds number and chamber configuration are not identical. Moreover, the present LES prediction successfully provides a dynamic picture of the instantaneous OTJ flow, which is qualitatively consistent with experimental deductions [7]. The similar instantaneous picture inside a chamber, however, cannot be obtained by experiment due to the complexity of the OTJ flow and also the constraint of those optical measurement techniques which are currently available. The key findings from the LES modeling are summarised below:

(1) The experimentally observed, asymmetric reattachment and continuous oscillation of a triangular jet issuing from a fluidic nozzle can be well predicted by LES. Consistent with earlier measurements, the prediction shows that some external fluid is induced due to the jet entrainment within the finite chamber, an inflowing stream, and joins the reverse fluid from the jet to form a secondary flow swirling against the oscillation direction.

(2)  The mean ratio of the out-flowing to inflowing volume flow rates at the exit plane of the chamber is estimated to be approximately 0.12.

(3)  The axis-switching phenomenon, often observed in non-circular free jets, occurs also in the simulated, partially confined and oscillating triangular jet. This was observed qualitatively in earlier experiments [7].

(4)  There are three strong longitudinal vortices emanating from the inlet plane between the vertices, observed previously by Lee [7], in the initial region at $x/D \leq 1$. The lowest static pressures of the OTJ flow are located at the centers of the longitudinal vortices. These three vortices appear to merge with the outer swirl near the location where the unmixed core region is ended.

# References

1. Luxton, R.E., Nathan, G.J.: Patent Application No PI4068/87, Australian Patent Office (1987)
2. Mi, J., Nathan, G.J., Luxton, R.E.: Family of oscillating jets. Pat App No. PCT/AU98/00959. (Granted worldwide)
3. Nathan, G.J., Mi, J., Alwahabi, Z.T., Newbold, G.J.R., Nobes, D.S.: Impacts of a jet's exit flow pattern on mixing and combustion performance. Pror. Energy Combust. Sci. **32**(5–6), 496–538 (2006)
4. Nathan, G., Hill, S., Luxton, R.: An axisymmetric 'fluidic' nozzle to generate jet precession. J. Fluid Mech. **370**, 347–380 (1998)
5. Mi, J., Nathan, G.J.: Self-excited jet-precession Strouhal number and its influence on downstream mixing field. J. Fluids Struct. **19**(6), 851–862 (2004)
6. Mi, J., Nathan, G.J., Wong, C.Y.: The influence of inlet flow condition on the frequency of self-excited jet precession. J. Fluids Struct. **22**(1), 129–133 (2006)
7. Lee S.K.: Study of a naturally oscillating triangular-jet flow. PhD thesis, School of Mechanical Engineering, The University of Adelaide, Australia. http://hdl.handle.net/2440/58581 (2009)
8. Lee, S., Lanspeary, P., Nathan, G., Kelso, R., Mi, J.: Low kinetic-energy loss oscillating-triangular-jet nozzles. Exp. Therm. Fluid Sci. **27**(5), 553–561 (2003)
9. England, G., Kalt, P., Nathan, G., Kelso, R.: The effect of density ratio on the near field of a naturally occurring oscillating jet. Exp. Fluids **48**(1), 69–80 (2010)
10. Germano, M., Piomelli, U., Moin, P., Cabot, W.: A dynamic subgrid-scale eddy viscosity model. Phys. Fluids A: Fluid Dyn. **3**, 1760 (1991)
11. Lilly, D.: A proposed modification of the Germano subgrid-scale closure method. Phys. Fluids A: Fluid Dyn. **4**, 633 (1992)
12. Fluent 6.3 Documentation. Fluent Inc (2007)
13. Pope, S.: Turbulent Flows, 1st edn. Cambridge University Press (2000)
14. Babu, P., Mahesh, K.: Upstream entrainment in numerical simulations of spatially evolving round jets. Phys. Fluids **16**, 3699 (2004)
15. Mi, J., Nobes, D.S., Nathan, G.J.: Influence of jet exit conditions on the passive scaler field of an axisymmetric free jet. J. Fluid Mech. **432**, 91–125 (2001)
16. Gutmark, E., Grinstein, F.: Flow control with noncircular jets. Annu. Rev. Fluid Mech. **31**(1), 239–272 (1999)
17. Mi, J., Kalt, P., Nathan, G.: On turbulent jets issuing from notched-rectangular and circular orifice plates. Flow Turbul. Combust. **84**(4), 565–582 (2010)

18. Quinn, W.: Measurements in the near flow field of an isosceles triangular turbulent free jet. Exp. Fluids **39**(1), 111–126 (2005)
19. Mi, J., Nathan, G.J., Luxton, R.E.: Centreline mixing characteristics of jets from nine differently shaped nozzles. Exp. Fluids **28**(1), 93–94 (2000)
20. Mi, J., Nathan, G.J., Luxton, R.E.: Mixing characteristics of a flapping jet from a self-exciting nozzle. Flow Turbul. Combust. **67**(1), 1–23 (2001)
21. Crow, S., Champagne, F.: Orderly structure in jet turbulence. J. Fluid Mech. **48**(03), 547–591 (1971)
22. Schadow, K., Gutmark, E., Parr, D., Wilson, K.: Selective control of flow coherence in triangular jets. Exp. Fluids **6**(2), 129–135 (2004)